Journal of Biomaterials Science, Polymer Edition

ISSN: 0920-5063 (Print) 1568-5624 (Online) Journal homepage: https://www.tandfonline.com/loi/tbsp20

PLinaS-g-PEG coated magnetic nanoparticles as a contrast agent for hepatocellular carcinoma diagnosis

Zeynep Karahaliloglu, Ebru Kilicay & Baki Hazer

To cite this article: Zeynep Karahaliloglu, Ebru Kilicay & Baki Hazer (2020): PLinaS-g-PEG coated magnetic nanoparticles as a contrast agent for hepatocellular carcinoma diagnosis, Journal of Biomaterials Science, Polymer Edition, DOI: 10.1080/09205063.2020.1764183

To link to this article: https://doi.org/10.1080/09205063.2020.1764183

Published online: 27 May 2020.

JOURNAL OF BIOMATERIALS SCIENCE, POLYMER EDITION
https://doi.org/10.1080/09205063.2020.1764183

PLinaS-g-PEG coated magnetic nanoparticles as a contrast agent for hepatocellular carcinoma diagnosis

Zeynep Karahaliloglu[a], Ebru Kilicay[b] and Baki Hazer[c,d,e]

[a]Faculty of Science, Department of Biology, Aksaray University, Aksaray, Turkey; [b]Vocational High School of Eldivan Health Care Services, Karatekin University, Cankiri, Turkey; [c]Department of Aircraft Airframe Engine Maintenance, Kapadokya University, Nevşehir, Turkey; [d]Department of Chemistry, Bülent Ecevit University, Zonguldak, Turkey; [e]Department of Nanotechnology Engineering, Bülent Ecevit University, Zonguldak, Turkey

ABSTRACT

Among many different types of fabricated nanoparticles, magnetic iron oxide nanoparticles (MNPs) have unique physical and chemical properties and have been widely used due to theirs enhanced permeability and retention effect for biomedical applications. The incorporated theranostic MNPs into biopolymer coatings are currently particular interest to investigators in the fields of nanobiomedicine because of efficiently delivering of various drugs, genes and providing imaging properties. Hepatocellular carcinoma (HCC) is the most prevalent reason of cancer-related deaths, makes it one of the worst malignant tumors in the world. Because, there is a lack of effective treatment methods for HCC, aforementioned magnetic carrier technology with recent innovations could be a promising tool in HCC diagnosis and treatment. Therefore, this study proposes a novel fatty-acid-based polymeric magnetic nanoprobe for diagnosis of hepatocellular tumors using polyethylene glycol (PEG)-terminated polystyrene (PS)-linoleic copolymer coated magnetic iron oxide nanoparticles. MNPs were synthesized by a co-precipitation method and were subsequently coated with a copolymer containing PEG group as termini. Fifty-nanometer-sized MNPs were incorporated into the core of PLinaS-g-PEG nanoparticles. The morphology and size distribution of the bare and magnetic PLinaS-g-PEG were determined by transmission electron microscopy (TEM), and dynamic light scattering (DLS), respectively. MTT and flow cytometry assays showed that PLinaS-g-PEG MNPs demonstrated ultrasentive apoptotic behavior against cancerous cell line, i.e. HepG2 in the culture plate when the fatty acid-containing polymer coated MNPs showed no adverse effect on L929 cell growth. The localization, and accumulation in hepatocytes of PLinaS-g-PEG MNPs without specific targeting ligand was confirmed by fluorescence and confocal microscopy. Therefore, PLinaS-g-PEG MNPs may be potentially used as a unique candidate for diagnosis of hepatocellular carcinomas.

ARTICLE HISTORY
Received 8 September 2019
Accepted 28 April 2020

KEYWORDS
Contrast agent; diagnosis; hepatocellular carcinoma; linoleic acid; nanoparticle

CONTACT Zeynep Karahaliloglu zeynokarahaliloglu@gmail.com Department of Biology, Aksaray University, Aksaray, Turkey.

Introduction

Hepatocellular carcinoma (HCC), known as hepatoma, is the most common primary liver cancer form diagnosed with late stage, and besides, the second most leading cause of cancer deaths worldwide [1]. As well as nonsurgical treatment methods of HCC such as chemoembolization, radiation, and ablation, surgical treatments is limited because the greater part of HCC cases are detected at an advanced stage [2]. In addition to the surgical- and nonsurgical options, a range of chemotherapeutic agents such as doxorubicin, mitomycin, cisplatin, epirubicin and sorafenib that is only available first-line systemic drug, have also been used for HCC treatment. Further, they have shown low clinical efficacy due to their nonspecific accumulation which lead to severe systemic side-effects and inadequate distribution in the body which causes insufficient dosage at the tumor site [3]. Therefore, there is a lack of efficient treatment of HCC. Nanomedicine could represent a promising solution for the prevention and treatment of HCC with several unique opportunities such as creating diagnostic and therapeutic functionalities *via* surface modification using specific HCC molecule targeting ligands and drugs [4].

Recently, superparamagnetic iron oxide nanocrystals (SPIONs) are getting increased attention due to their impressive activity in biomedical fields including targeted drug delivery, diagnosis *via* magnetic resonance imaging, tissue engineering, bioseparation, and nanoparticle-mediated hyperthermia in cancer therapy [5,6]. Surface functionality is the most critical parameter for the successful development of well-interacted SPIONs with biological systems. Modification of SPION surface with bioactive molecules directly improve the biological activities such as cellular uptake, bio-distribution, blood circulation, and metabolism of nanoparticles [7–10]. These surface coatings can increase the targeting specificity of nanoparticles [11], provide specifically illumination at the targeted tissue when is used as a contrast agents [12], and do not allow unwanted interaction with healthy tissue [13]. Therefore, SPIONs are typically surface-modified or coated with biocompatible polymers such as dextran, poly-ethylene glycol (PEG), alginate, and pullulan [14–16].

Ideally, a SPIONs formulation should prevent the rapid clearance from the blood by the reticular endothelial system (RES), and the physical properties or magnetization property of the core material should not affect the drug loading ability of formulation and the formulation is capable to conjugate with a ligand or antibody. Furthermore, the above-mentioned coating materials should improve the cellular biocompatibility and increase half-life in the bloodstream by minimizing the protein absorption on the SPIONs surface besides providing a colloidal stability in physiological media [17,18]. Especially, PEG is frequently used as a coating agent because of its hydrophilicity, nontoxicity and absence of antigenicity and immunogenicity [19]. The molecule prevents phagocytic capture of SPIONs by cellular members of the immune system and tends to circulate for longer times when administered intravenously. Furthermore, due to PEG's enhanced permeability and retention (EPR) effect, PEG-coated-SPIONs can penetrate preferentially into tumor tissue due to a leaky tumor vasculature and poor lymphatic drainage, and retained there [20]. Currently, RES-targeted iron oxide-based contrast agents are used to prevent the accumulation of nanoparticles. For example, Khandar et al. found that colloidal stability of SPION

after PEG-modification enhanced with the increasing PEG's molecular weight. In addition to the stability effect of PEG, the blood circulation evaluations in mice demonstrated that the t1/2 of SPIO tracers varied with both PEG's molecular weight and loading [21]. Therefore, PEG-modification of SPIONs' surface comes with a number of privileges.

Most recently, besides the RES-mediated contrast agents, different methods such as hepatocyte selective agents for HCC treatment have been investigated. Hepatocyte-selective contrast agents could be promising tool in the evaluation of hepatic function with a high specific hepatic affinity. It is well known that essential polyunsaturated fatty acids (PUFAs) accumulate in hepatocytes and have a primary role in cholesterol and triglyceride synthesis, and linoleic acid (LA) is also one of the most common PUFAs [22,23]. There are a lot of studies related to hepatocyte affinity of PUFAs. For instance, Yotsumoto et al. showed that one of the conjugated linoleic acid (CLA)-isomer suppressed cellular cholesterol and triglyceride synthesis in HepG2 cells [24]. Pandey and colleagues also reported that LA-enriched phospholipids stimulate hepatic apolipoprotein A-I secretion in HepG2 cells and human primary hepatocytes [25]. These findings mean that LA could improve specific affinity of nanocarriers against hepatocytes and also these carriers owing to hydrophobic carbon chain can be easily combined with a hydrophilic polymer as a diagnostic tool.

Herein, we developed a magnetic iron oxide nanoparticle (MNP) formulation contains an iron-oxide core and PLinaS-g-PEG-coating layer as a hepatocyte-targeting contrast agent. It was hypothesized that PLinaS-g-PEG-coating of MNPs due to LAs component would enhance the accumulation of nanoparticles in the liver through lipid metabolism as a hepatocyte-targeting contrast probe, and this provides a targeted detection ability of hepatocellular carcinomas. Another novelty of the study is that we examined the effect of synthesized nanoparticles on the growth of hepatocellular carcinoma cells and respective normal connective tissue cells i.e. L929 though many studies did not consider the effect of fatty acid e.g. linoleic acid on normal cells. Moreover, PEG-content of these MNPs would prevent their rapid clearance by the RES besides enhancing their water dispersity and steric stability. Further, the conjugation of antibody or targeting ligands to the structure can easily be realized due to the functionalized groups on PEG-termini in future studies.

Materials and methods

Materials

Phosphate-buffered saline (1× PBS), Octadeca-9,12-dienoic acid (linoleic acid), Live/Dead Cell Double Staining kit, iron (III) chloride, iron (II) chloride, MTT (3-[4,5-dimethylthiazol-2yl]-2,5-diphenyl-tetrazolium bromide) reagent and paraformaldehyde were purchased from Sigma–Aldrich (St Louis, MO, USA). Dulbecco's modified Eagle's medium (DMEM), penicillin–streptomycin solution, fetal bovine serum (FBS), and TACS Annexin V-Fluorescein Apoptosis Detection Kit were supplied from Biological Industries (Israel), and R&D Systems, Inc., (MN, USA), respectively. Cholesterol assay kit was purchased from Abcam. All other chemicals were used directly without further purification.

Methods

Cell culture

HepG2 (ATCC HB-8065) and L929 (ATCC CCL-1) cell lines were purchased from American Type Culture Collection. L929 was also cultured in cell growth medium (RPMI) while HepG2 cells were cultured in low glucose DMEM medium supplemented with 10% (*v*/*v*) FBS, 1% penicillin and 1% streptomycin. The cells were routinely passaged once a week under standard cell culture conditions and maintained at 37 °C.

Synthesis of PLinaS-g-PEG graft copolymer

Autoxidation process of soya oil was carried out according to previously established protocol [26]. Initially, 12.7 g of linoleic acid was spread out in a Petri dish ($U = 14$ cm, oil thickness: 0.8 mm), and then subjected to daylight at room temperature for ca. 4 weeks. A yellow viscous polymeric linoleic acid (PLina) was obtained, and the soluble part of the PLina was extracted using chloroform.

PS-g-PLina graft copolymer was synthesized by free radical polymerization of styrene. For this purpose, argon gas flowed into flask, which contains 0.5 g of PLina, and 8.0 g of styrene, at 95 °C for 5 h. After stopping reaction, the obtained polymer was dissolved in chloroform, and precipitated in methanol and then, the graft copolymer was filtered, and dried under vacuum at 40 °C for 24 h following drying at room temperature.

For the synthesis of PLinaS-g-PEG, as long as 1.05 g of PLina and 3.04 g of $PEG1000NH_2$ were dissolved in a 10 mL-volumetric flask using toluene, the argon gas passed through the flask at 95 °C for 5 h. The solvent was quickly evaporated at the end of process. After precipitation step with methanol, the gained polymer was dried at room temperature overnight. For further purification studies, the crude polymer was soaked into distilled water to remove unreacted PEG-molecules. The pure PLinaS-g-PEG graft copolymer was filtered, and dried under vacuum at 40 °C for 24 h.

The synthesized pure polymer was characterized by attenuated total reflectance–Fourier transform infrared spectroscopy (ATR–FTIR, Perkin-Elmer SpectrumOne, Nicolet 520, USA) with a spectral range of 500–4000 cm^{-1} and ^1H-nuclear magnetic resonance (H-NMR, Bruker DPX-4,00,400-MHz High-Performance Digital FT-NMR Spectrometer, Karlsruhe, Germany).

Synthesis of MNPs

MNPs were synthesized according to protocol reported in our previous work [27]. Fifty nanometer MNPs were synthesized by co-precipitation method. Initially, $FeCl_2{\cdot}4H_2O$ and $FeCl_3{\cdot}6H_2O$ were dissolved in water in 1:2 molar ratio and then, an aqueous NH_3 solution (4 M) was then added dropwise to the above solution under nitrogen protection and under constant magnetic stirring at room temperature. After stirring continuously for 1 h, the brownish yellow solution was separated by centrifugation at 9000 r/min for 30 min at room temperature, and washing of the particles was repeated several times with water to remove of any residual salts, which was used during the co-precipitation. The final product was then dried in a vacuum oven for several hours.

Table 1. The compound of PLinaS-g-PEG NPS created at different MNPs ratios.

Sample	Component (Polymer/MNPs ratio, w/w%)
MNPs	0:100
PLinaS-g-PEG NPs	100:0
5PLinaS-g-PEG-MNPs	66:34
7PLinaS-g-PEG-MNPs	53:47
10PLinaS-g-PEG-MNPs	50:50

Preparation of bare PLinaS-g-PEG NPs

PLinaS-g-PEG NPs were prepared for the study using single-emulsion solvent evaporation technique as follows: A solution of PLinaS-g-PEG in dichloromethane (1 mg/mL, w/v) was prepared and the solution was then emulsified in 50 mL of 6% w/v Tween-80 solution by sonication over an ice bath using a probe sonicator (T 125 Digital Ultra Turrax Homogenizer; IKA, Germany). The sonication was continued for 2 h to evaporate of organic solvent. After that, the particles were collected by centrifugation (Centrifuge 5810 R; Eppendorf, Germany) at 12,000r/min for 30 min, the supernatant decanted off and then, washed with deionized water for three times. Finally, the obtained NPs were freeze-dried and used for further experiments.

Preparation of PLinaS-g-PEG coated MNPs

PLinaS-g-PEG coated MNPs were also prepared by the same procedure. Briefly, as the compound of samples shown in Table 1; 5, 7 and 10 mg of the synthesized MNPs and 10 mg of PLinaS-g-PEG were suspended in 1 ml ethanol and 9 ml dichlorometane (Sigma), respectively. Both solutions were collected in a single tube. The initial organic phase was added dropwise to 50 ml of 1.5% (w/v) Tween-80 using a sonicator probe at 90% amplitude, and allowed to mechanically stir for 2 h. PLinaS-g-PEG MNPs were isolated by centrifugation at 12,000 rpm for 20 min and washed thrice with dH_2O.

Characterization of bare and magnetic PLinaS-g-PEG-NPs

Nanoparticle morphology was characterized by transmission electron microscopy (TEM) (Hitachi HT7800) with accelerating voltage of 80 kV. The aggregation and polydispersity of particles were characterized using dynamic light scattering (DLS) using Malvern Instruments, Model 3000 HSA, England. The infrared spectra were recorded in the range 4000–500 cm^{-1} on a Fourier transform infrared spectrometer (FTIR, Perkin Elmer SpectrumOne, Nicolet 520, USA).

Electron spin resonance spectrometer (ESR) measurements to verify the superparamagnetic behavior of the nanoparticles were recorded with a Bruker ELEXSYS E580 spectrometer operating at frequency 9.2 GHz. The measurements were carried out at room temperature.

In vitro magnetic resonance imaging

The uncoated and coated MNPs samples were scanned under a 3 T Siemens Magnetom Tim Trio MRI scanner, 32-channel head coil. T1-weighted and T2-weighted images were obtained using the following parameters, respectively: TI = [24, 100, 200, 400, 600, 650, 700, 750, 800, 850, 900, 950, 1000, 1250, 1500, 1900] ms,

TR = 2000 ms, TE = 11 ms, slice thickness = 4 mm, field-of-view (FOV) = 160 × 160 mm, resolution = 1.25 × 1.25 mm. For T2 values, TE = [10, 15, 20, 25, 30, 40, 50, 60, 80, 100, 125, 150, 200 250, 300, 400, 500, 600, 800, 1000] ms, TR = 3000 ms, slice thickness = 4 mm, FOV = 160 × 160 mm, resolution = 1.25 × 1.25 mm. To calculate r1 and r2 relaxivities in an aqueous solution, MNPs were suspended in tubes with water using 0.05–0.8 mM concentration range. r2 maps (r2 = 1/T2) were calculated using an in-house script developed in Matlab (Mathworks, Natik, MA, USA).

In vitro cytotoxicity assay

MTT cell viability assay was realized to determine the toxicity of uncoated and coated MNPs. Initially, the cells were seeded in 96-well plate at a density of 9×10^3 cells/well and incubated overnight before the nanoparticles were applied. Twenty-four hours later, the old medium was removed and replaced with fresh medium containing PLinaS-g-PEG NPs or PLinaS-g-PEG MNPs in a range of concentrations at 25, 50, 100 and 200 μg/ml (Bare PLinaS-g-PEGNPs, 5PLinaS-g-PEG MNPs, 7PLinaS-g-PEG MNPs, 10PLinaS-g-PEG MNPs), while culture media alone without nanoparticles accepted as a control. After 24 h incubation, the medium was aspirated and the cells were washed three times with PBS (pH 7.0). Then, 200 μL of the reaction solution (MTT reagent) were added to each well and the plate was incubated at 37 °C, 5% CO_2 for 4 h. After the end of incubation, the medium was replaced with isopropanol/HCl mixture and the optical density at 570 nm was measured using a microplate reader (Biochrom Asys Expert Plus. Microplate Reader, Holliston, MA). Absorbance value of the control group was equated to 100% and the rest of the values were normalized to the control group.

To support the obtained MTT assay data, a double staining assay was performed. HepG2 and L929 (5×10^3 cells/well) cells were grown in a 24 well plate overnight and incubated with 25 μg/mL extraction medium of PLinaS-g-PEG nanoparticles. After 3 h of incubation in CO_2 incubator at 37 °C, the cells were washed with PBS (pH 7.4), stained with Calcein-AM and ethidium homodimer-1 (EthD-1) following kit manufacturer's instructions. Briefly, cells were stained with 100 μl of Calcein-AM/ethidium homodimer-1 (EthD-1) cocktail for 5 min at room temperature, the cells were then observed by imaging using fluorescence microscope (Leica, Germany) including Texas Red and fluorescein (FITC) filters.

Prussian blue staining for iron detection

Imaging of PLinaS-g-PEG MNPs-labeled cells was performed by Prussian blue staining. Initially, the cells were incubated with a nanoparticle solution at a concentration of 25 μg/mL for 3 h, and then the cells were washed with PBS to remove nanoparticle residues. Following several washes, the cells were fixed with 4% paraformaldehyde in PBS for 10 min. For staining procedure, they were incubated with Prussian blue (10 wt%) and mixture of Prussian blue and 20% HCl solution in ratio of 1:1 for 5 and 30 min, respectively. After washing with PBS, they were counterstained using neutral red solution (0.05%) for 5 min. The stained cells were observed under an inverted optical microscope at 20x magnification.

Flow cytometry analysis

Evaluation of nanoparticle uptake was carried out using a fluorescence-activated cell sorting analysis and data were analyzed using BD FACSDiva software. Initially, HepG2 and L929 cells (1×10^5 cells/mL) treated with a dose (25 μg/mL) of NPs for 24 h in CO_2 incubator at 37 °C, and the apoptotic assay was performed according to the manufacturer's instructions. Briefly, the cells were trypsinized and centrifuged at 3500 rpm for 5 min. Then, the cells were washed several times with PBS. Finally, the cell pellets were resuspended in 400 μL binding buffer and stained with 100 μL of incubation reagent which include 1 μL annexin V-FITC, 10 μL of PI, and buffer solution for 15 min in the dark, and fluorescence signals were measured *via* flow cytometry.

Characterization of cellular uptake of nanoparticles by confocal microscopy

Confocal microscopy was performed on a LSM 800 confocal laser-scanning microscope (Jena, Germany). HepG2 and L929 cells were seeded on lean cover-slips placed in a 24 well-plate at 1×10^2 cells per cover-slip with 200 μL of medium per chamber. The cells were allowed to grow overnight, and then the medium was replaced with extraction medium (25 μg/mL) as mentioned in the section of *in vitro* cytotoxicity assay. The cells were incubated with extraction medium of NPs for 3 h, and then the medium was removed, and the cells were washed three times with phosphate buffer solution (PBS, pH = 7.4). For the confocal studies, the cells were fixed at 4 °C for 10 min using paraformaldehyde solution (4 w/v % in PBS), and the images were obtained.

Cholesterol and triglyceride analysis

Qualitative estimation of membrane cholesterol in HepG2 and L929 cells was performed by cholesterol assay Kit (Abcam, ab133116). Previously, the cells were grown in a 24 well plate at 3×10^4 cells/well, and incubated overnight. The cells were exposed to the nanoparticle extraction medium (25 μg/mL) for 3 h and subsequently, the medium was removed from the wells, and the cells were fixed with Cell-Based Assay Fixative Solution for 10 min. Thereafter, the cells were washed three times with buffer, and stained with filipin III solution in the dark for 1 h, and the images were collected by fluorescent microscopy using an excitation of 340–380 nm and emission of 385–470 nm.

Statistical analysis

Data were presented as means ± SD. Statistical evaluations between groups were conducted by one way ANOVA and Student's *t*-test. Statistically significant value was set at $p < 0.05$.

Results and discussions

Characterization of PLinaS-g-PEG copolymer

The graft copolymers containing primary amine terminal were synthesized *via* three steps. First, linoleic acid was autoxidized under daylight in order to obtain a macro

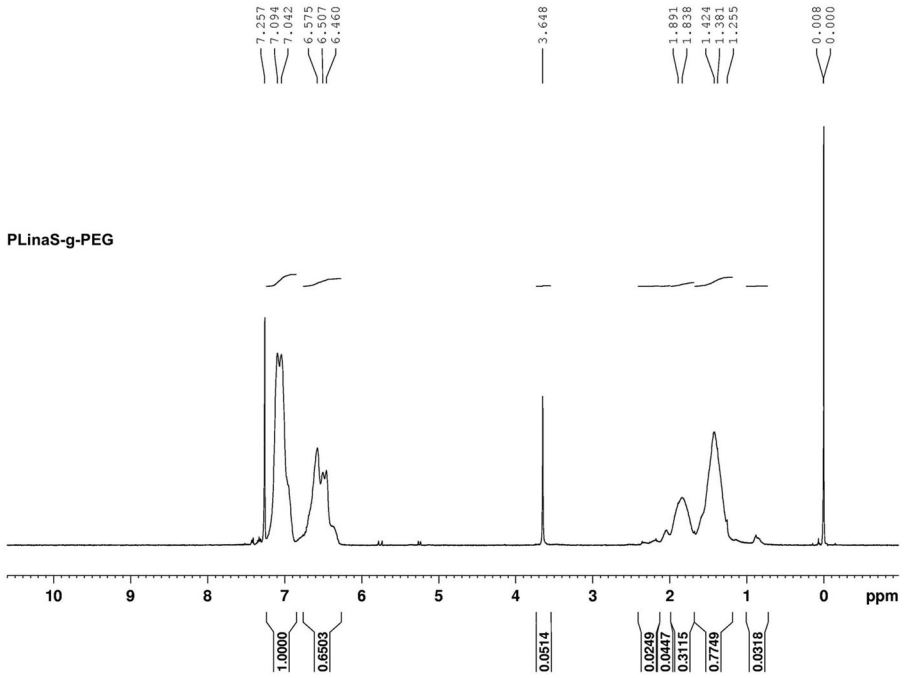

Figure 1. ^{1}H-NMR spectra of PLinaS-g-PEG copolymer.

peroxide initiator (PLina). Styrene that includes free carbocyclic acid groups was polymerized by free radical polymerization technique *via* PLina. Then, PEG was reacted with the carbocyclic acid groups of polystyrene (PS)-g-PLina graft copolymer to produce PS-g-PLina-g-PEG rod-coil tadpole amphiphilic graft copolymer [26]. Characterization of PLinaS-g-PEG graft copolymer was performed by using FTIR, and ^{1}H NMR techniques. Their ^{1}H NMR spectra are presented in Figure 1. The signals between 6.2 and 7.6 ppm assigned to phenyl group of PS. The broad peak at 3.6 ppm was attributed to the –CH–O– groups of PLina and PEG terminal end.

According to the FTIR spectra in Figure 2, the sharp peak at 1709 and 1597 cm^{-1} was attributed to C = O stretching and phenyl group of PLina and polystyrene, respectively. After PEGylation, the peak that appeared at 1100 cm^{-1} was from ether band of PEG terminal end, which confirmed successful PEGylation of (PS)-g-PLina graft copolymer.

In the next step, PLinaS-g-PEG NPs having magnetic and non-magnetic properties were synthesized by emulsion/solvent evaporation method. TEM images of PLinaS-g-PEG-NPs obtained at a Tween-80 concentration of 0.6% wt/vol, polymer concentration of 0.1% wt/vol, and sonication amplitude of 90%, are shown in Figure 3A., and the observed bare PLinaS-g-PEG-NPs have a solid spherical morphology with an average size 202 nm.

PLinaS-g-PEG-coated MNPs were obtained with the aforementioned nanoparticle preparation technique after superparamagnetic iron oxide nanoparticles were synthesized by coprecipitation method as previously established protocol [27]. The surface morphologies and sizes of PLinaS-g-PEG-MNPs containing different ratio of MNPs

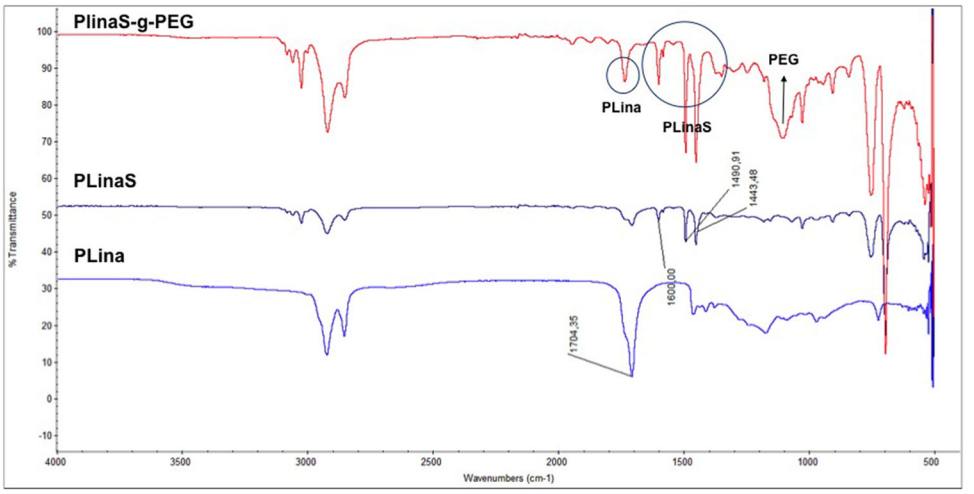

Figure 2. FTIR spectra of PLinaS-g-PEG copolymer.

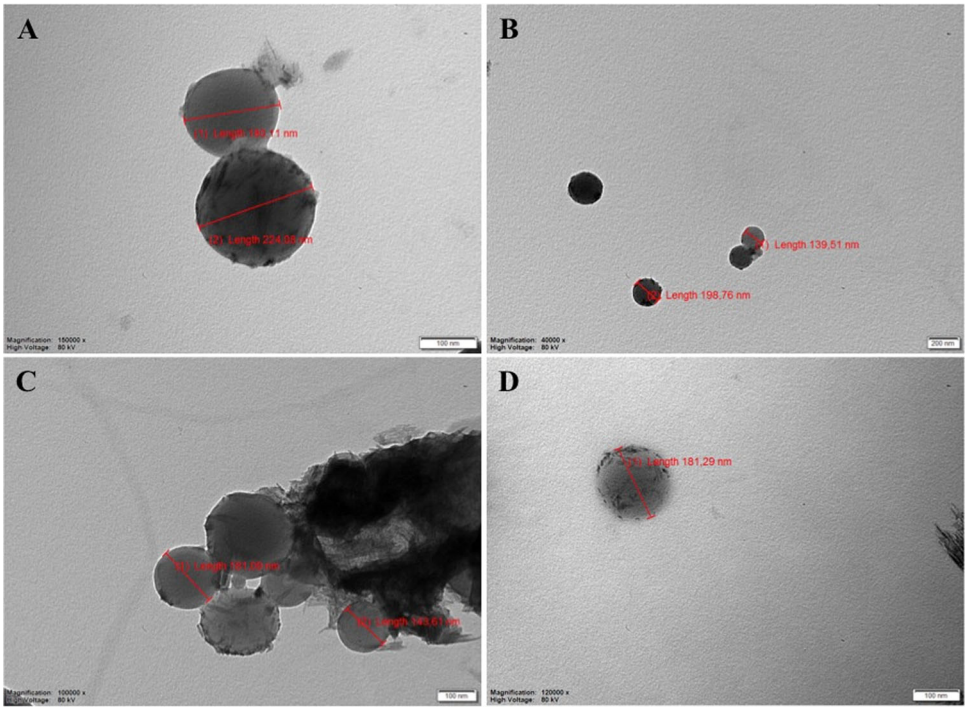

Figure 3. TEM images of PLinaS-g-PEG-NPs (A) and 5PLinaS-g-PEG-MNPs (B), 7PLinaS-g-PEG-MNPs (C), 10PLinaS-g-PEG-MNPs (D). Scale bars, 100 and 200 nm.

were observed by TEM. From the image, magnetic nanoparticles are spherical with a mean size around 168, 162, and 181 nm for 5PLinaS-g-PEG-MNPs, 7PLinaS-g-PEG-MNPs, and 10PLinaS-g-PEG-MNPs, respectively.

The particle size distribution of PLinaS-g-PEG NPs and PLinaS-g-PEG-MNPs was characterized by DLS. The effect of the concentration variation of MNPs on the size,

Table 2. Physicohemical properties of PLinaS-g-PEG-NPS. The mean ± SD for three replicates is illustrated.

Sample	Size (nm)	Polydispersity Index (PDI)	Zeta Potential (mV)
MNPs	52 ± 2.3	0.05 ± 0.002	1.32 ± 0.09
PLinaS-g-PEG NPs	148 ± 7.8	0.14 ± 0.05	4.76 ± 0.2
5PLinaS-g-PEG-MNPs	170 ± 8.5	0.29 ± 0.04	0.35 ± 0.07
7PLinaS-g-PEG-MNPs	185 ± 10.2	0.34 ± 0.07	0.45 ± 0.05
10PLinaS-g-PEG-MNPs	202 ± 11.4	0.35 ± 0.09	0.69 ± 0.07

polydispersity index and zeta potential of PLinaS-g-PEG nanoparticles was investigated. The DLS data obtained by varying MNPs concentrations was shown in Table 2. According to the DLS results, we found that the hydrodynamic diameters of PLinaS-g-PEG-MNPs are larger than from naked NPs (148 ± 7.8, 170 ± 8.5, 185 ± 10.2, and 202 ± 11.4 nm for PLinaS-g-PEG-MNPs, 5PLinaS-g-PEG-MNPs, 7PLinaS-g-PEG-MNPs, and 10PLinaS-g-PEG-MNPs, respectively), and the size of nanoparticles became bigger by increasing the MNPs concentration. Varshosaz et al. prepared MNPs coated with oleic acid (OA), and encapsulated within the micelles. The particle size of theirs grew after entrapping of MNPs into copolymeric micelles [28]. Further; it was found that measurements by DLS are slightly smaller when compared to TEM, the obtained size difference can be attributed to the local measurement capability of TEM analysis, i.e. the analysis could not catch the smaller particles. Furthermore, it was confirmed by study that the measurements obtained by DLS presented more accurate results when compared to TEM [29].

Furthermore, as shown in Table 2, the zeta potential of all NPs formulations was positive. The observed surface charge is the most important parameter for imaging, gene transfer, and drug delivery because nanoparticles having a net positive charge can easily penetrate into negatively charged plasma membrane of the target cells compared negatively charged ones due to their stronger coulombic interactions [30,31]. Due to the fact that PLinaS-g-PEG particles could successively interact with the cells surface toward a positive zeta potential.

Figure 4 shows the FTIR spectra of magnetic- and nonmagnetic PLinaS-g-PEG NPS. For magnetite nanoparticle formulations, the obtained absorption peaks at 520 cm^{-1} were attributed to the Fe–O stretching of Fe_3O_4, and especially, the intense peak can be associated with Fe ions coming from core of PLinaS-g-PEG [32,33]. In the curve, the peaks observed at 1704/1600 cm^{-1} and 1100 cm^{-1} are typical linoleic acid, polystyrene and PEG signals, respectively. From the above observation, we can confirm that magnetic core was encapsulated into PLinaS-g-PEG matrix.

ESR analysis

To confirm the super paramagnetic behavior, we conducted ESR analysis on these nanoparticles. The room-temperature ESR spectra of the lyophilized 5PLinaS-g-PEG-MNPs, 7PLinaS-g-PEG-MNPs, 10PLinaS-g-PEG-MNPs are shown in Figure 5. The g values are found to be 2.29, 2.28 and 2.30 for 5PLinaS-g-PEG-MNPs, 7PLinaS-g-PEG-MNPs, 10PLinaS-g-PEG-MNPs. As can be seen from ESR spectra (Figure 5), the resonance absorption peaks of all three samples showed broad peak intensity while

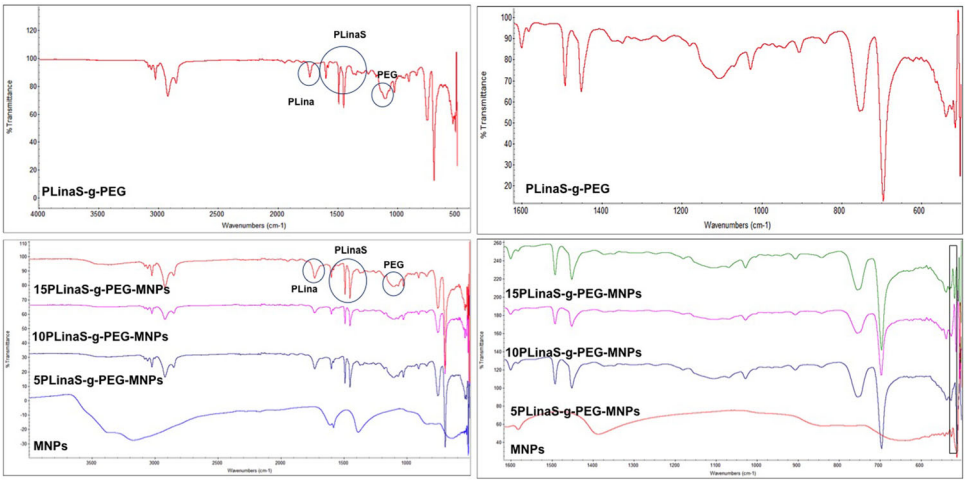

Figure 4. FTIR spectra of PLinaS-g-PEG-NPs, MNPs, 5PLinaS-g-PEG-MNPs, 7PLinaS-g-PEG-MNPs, and 10PLinaS-g-PEG-MNPs.

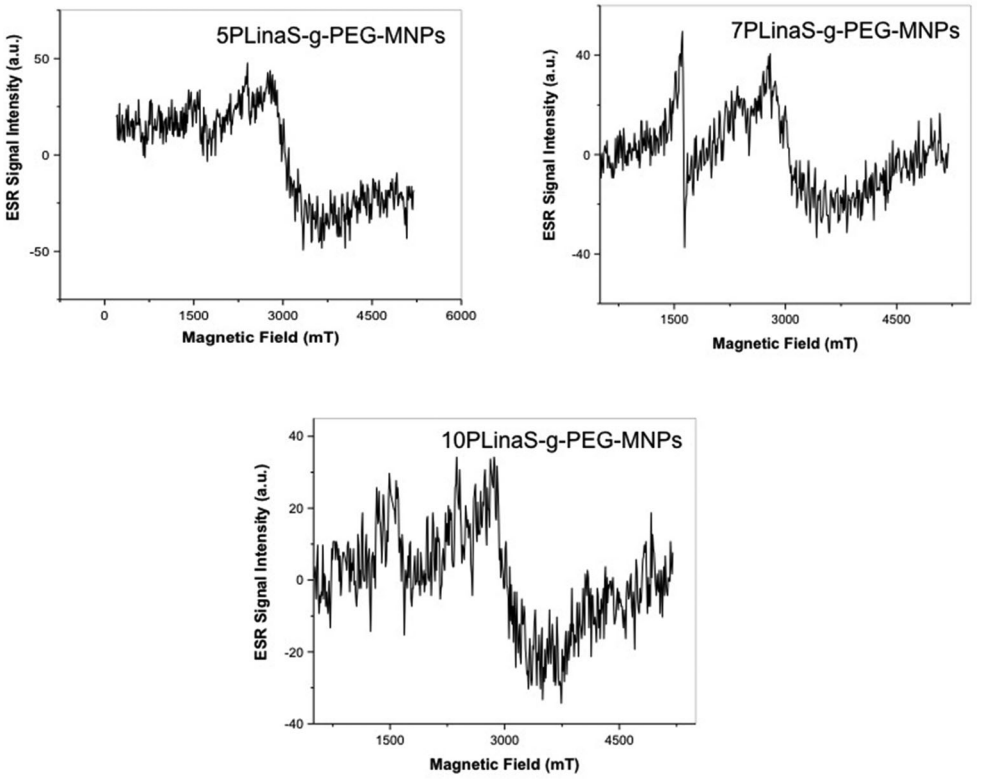

Figure 5. ESR spectra of 5PLinaS-g-PEG-MNPs, 7PLinaS-g-PEG-MNPs, and 10PLinaS-g-PEG-MNPs.

there is no considerable variety related to magnetic behavior of commercial MNPs, and PLinaS-g-PEG-MNPs. This suggests the superparamagnetic characteristic of PLinaS-g-PEG-MNPs as reported in the literature [34,35].

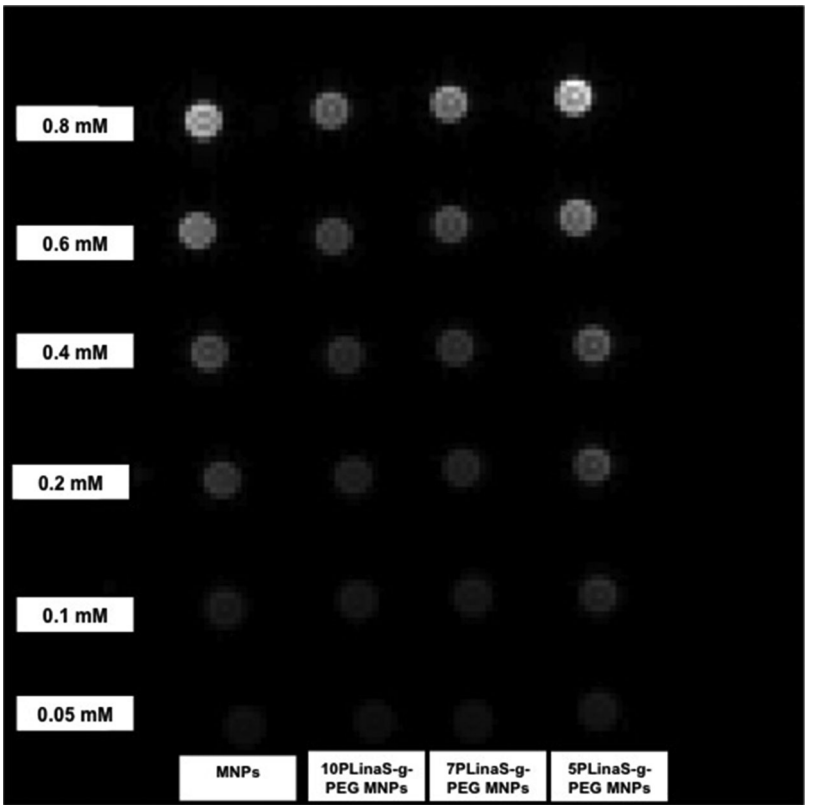

Figure 6. T2-weighted MRI images of 5PLinaS-g-PEG-MNPs, 7PLinaS-g-PEG-MNPs, and 10PLinaS-g-PEG-MNPs.

In vitro magnetic resonance imaging

To investigate the effect of PLinaS-g-PEG coating on MRI signal-enhancement, a phantom test was carried out. Figure 6 shows T2-weighted MRI images of various concentrations of PLinaS-g-PEG-coated MNPs in water. It can be seen that T2-weighted MR images of 10 PLinaS-g-PEG-MNPs were darker than those of either the PLinaS-g-PEG NPs coated with lower Fe_3O_4 concentrations. Further, MRI signal intensity enhanced significantly with increasing MNPs concentration in water.

Since MNPs are T2-type (negative) contrast agents in MRI, the spin-spin relaxation rate, $1/T_2$, was calculated and shown in Figure 7. For 5, 7, and 10PLinaS-g-PEG-coated MNPs, the r_2 values were 0.396 $mM^{-1}\,sec^{-1}$, 0.532 and 1.309 $mM^{-1}\,sec^{-1}$, respectively, at 3 T. The 10PLinaS-g-PEG-coated MNPs showed an enhanced relaxivity of $r_2 = 1.309\ mM^{-1}\,sec^{-1}$ in DI H_2O, at 3 T. The comparison of the relaxivity changes of varying MNPs core formulations coated with PLinaS-g-PEG demonstrated that while the core concentration was increased, r_2 was increased. These obtained relaxivity values were comparable with previous reports of other counterpart MRI contrast agents. For instance, Mu *et al.* reported BSA-coated GA-Fe (gallic acid (GA)–Fe(III) coordination polymer) (GA-Fe@BSA) NPs with a 3.5 nm for cancer theranostic applications [36]. Relaxivity values of these NPs for r1 and r2 are 0.89 mM/second and 0.95 mM/second,

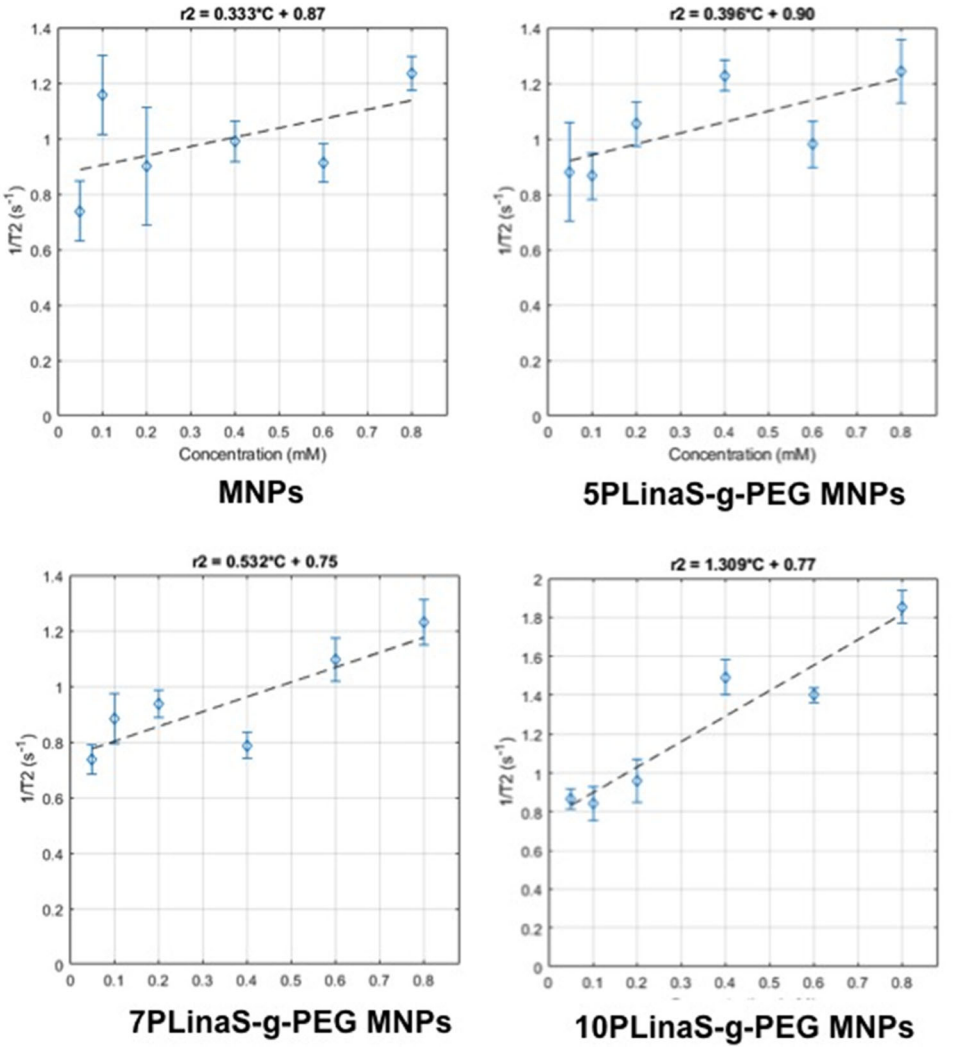

Figure 7. The r_2 values of MNPs, 5PLinaS-g-PEG-MNPs, 7PLinaS-g-PEG-MNPs, and 10PLinaS-g-PEG-MNPs.

respectively. These results confirmed that PLinaS-g-PEG-coated MNPs would provide good T2-weighted contrast.

In vitro cytotoxicity assay

PLinaS-g-PEG-NPs or -MNPs cytotoxicity was tested *in vitro* using an MTT assay, and all results were given in Figure 8. It shows cell viability results of increasing amount of NPs formulations for HepG2 and L929 cells after 24 of incubation. As can be seen in Figure 8A, for HepG2 cell types, the cytoxicity value of cells treated with 5, 7 and 10PLinaS-g-PEG MNPs are 53.4, 55.7, and 48.4%, respectively, while cells after incubation with 200 μg/mL of MNPs and naked PLinaS-g-PEG-NPs for 24 h are approximately 48.9 and 66.95% viable, respectively. The cell viability of MNPs

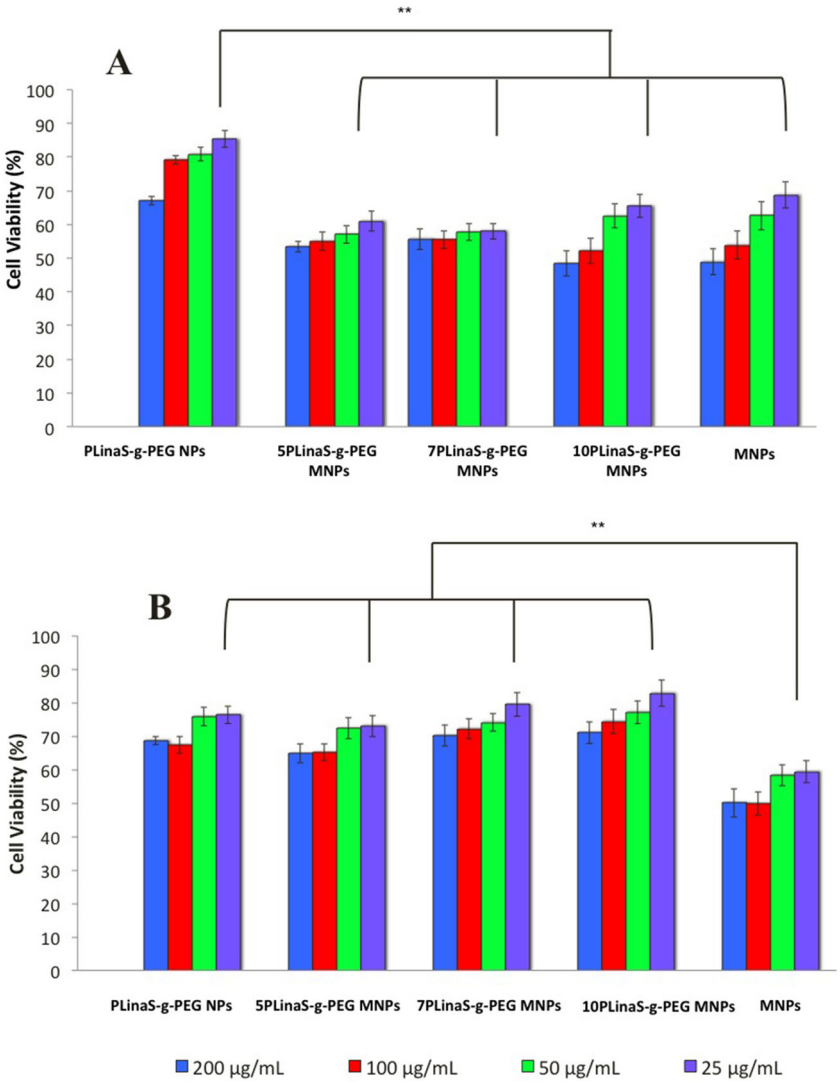

Figure 8. The *in vitro* cytotoxicity of PLinaS-g-PEG-NPs or -MNPs. The cell viability of HepG2(A) and L929 cells (B) after 24-h treatment of NPs with different concentrations were measured by MTT assay. Values are mean ± SEM; $n = 3$.

encapsulated nanoparticles decreased with increasing magnetite concentration, and the cytotoxicity of PLinaS-g-PEG-MNPs effectively increased against HepG2 compared with naked PLinaS-g-PEG-NPs (*, $p < 0.05$). Furthermore, PLinaS-g-PEG-MNPs showed a dose-dependent cytotoxicity against HepG2 cancer cells in the range of test concentration (25–200 µg/mL). The decrease in the cell viability can be associated with interaction between subcellular membrane molecules and the affected metabolism [37,38].

While PLinaS-g-PEG-NPs or -MNPs was treated with L929 cells, which is the most frequently used healthy cell line, as can be seen in Figure 8B, the encapsulated

MNPs and naked PLinaS-g-PEG-NPs showed similar viability following exposure. Further, MNPs with increasing concentration caused a progressive toxic effect at the tested concentrations. However, the difference in cell viability of coated- and uncoated MNPs formulations is significant (*, $p < 0.05$). Thus, the effect of the surface coating material would be the best proof for non-toxic properties of PLinaS-g-PEG-MNPs, and the cell viability may be improved by PEG-terminal end on the surface of polymer-coating materials. Bae and coworkers investigated the biocompatibility of different coated Fe_3O_4, $ZnFe_2O_4$ and $NiFe_2O_4$ nanoparticles [39]. Giri et al. studied the comparatively toxic effect of $MnFe_2O_4$ in contrast with Fe_3O_4 [40]. All of studies demonstrated that threshold biocompatibility concentration for biomedical applications is highly depend on the nature, structure, size and surface coating of ferrites [41]. Furthermore, the study performed by Jeng and Swanson showed major effect of SPIONs on the mitochondrial function [42]. Au et al. also found similar results and they deduced that SPIONs altered mitochondrial functions besides decreased cell viability [43].

To support MTT data, live/dead cell rate induced by PLinaS-g-PEG-NPs was further investigated by calcein AM and ethidium bromide staining. After 3-h exposure, HepG2 cells displayed positive PI staining, while only a small portion of nuclei of L929 cells treated with nanoparticles showed positive PI staining, which was the sign of high cell viability (Figure 9). On the other hand, the images obviously demonstrated that PLinaS-g-PEG-MNPs mainly accumulated in HepG2 cells. This effect can be assigned to nonspecific targeting feature of linoleic acid to various tumor cells *in vitro* and *in vivo* and PEG usage as a passive targeting tool in cancer treatment [44,45]. Besides that, MNPs encapsulated with PLinaS-g-PEG showed more protective effect on L929 compared to HepG2 cells because the normal cells are less affected by LA conjugation while naked MNPs led to acute toxicity for both cell line, i.e. HepG2 and L929 [46]. Furthermore, the MNPs concentration-dependent cytotoxicity for both cell lines was clearly confirmed in Fig. 9.

Prussian blue staining

To confirm PLinaS-g-PEG-MNPs localization in hepatocytes and mouse fibroblasts, Prussian blue staining was conducted. An ideal marker should show high specificity towards cancer cells contrary to normal cells. As can be seen in Figure 10, PLinaS-g-PEG-MNPs were mainly observed in the cytoplasm and perinuclear region of cells. Prussian blue staining revealed that nanoparticles subsequently internalized by hepatocellular carcinoma cells and carcinoma-associated stromal cells, i.e. fibroblast cells which assist in distribution and retention of the nanoparticles into the tumor site. Yang et al. designed urokinase plasminogen activator receptor (uPAR) targeted dual-modality molecular imaging nanoparticle probe using functionalized MNPs, and they examined the accumulation of these nanoparticles on the uPAR-expressing human pancreatic cancer (MIA PaCa-2) and mouse endothelial cell lines (MS1) [47]. According to Prussian blue staining images, they were observed in the cytoplasm of MIA PaCa-2 and MS1 mouse endothelial cells.

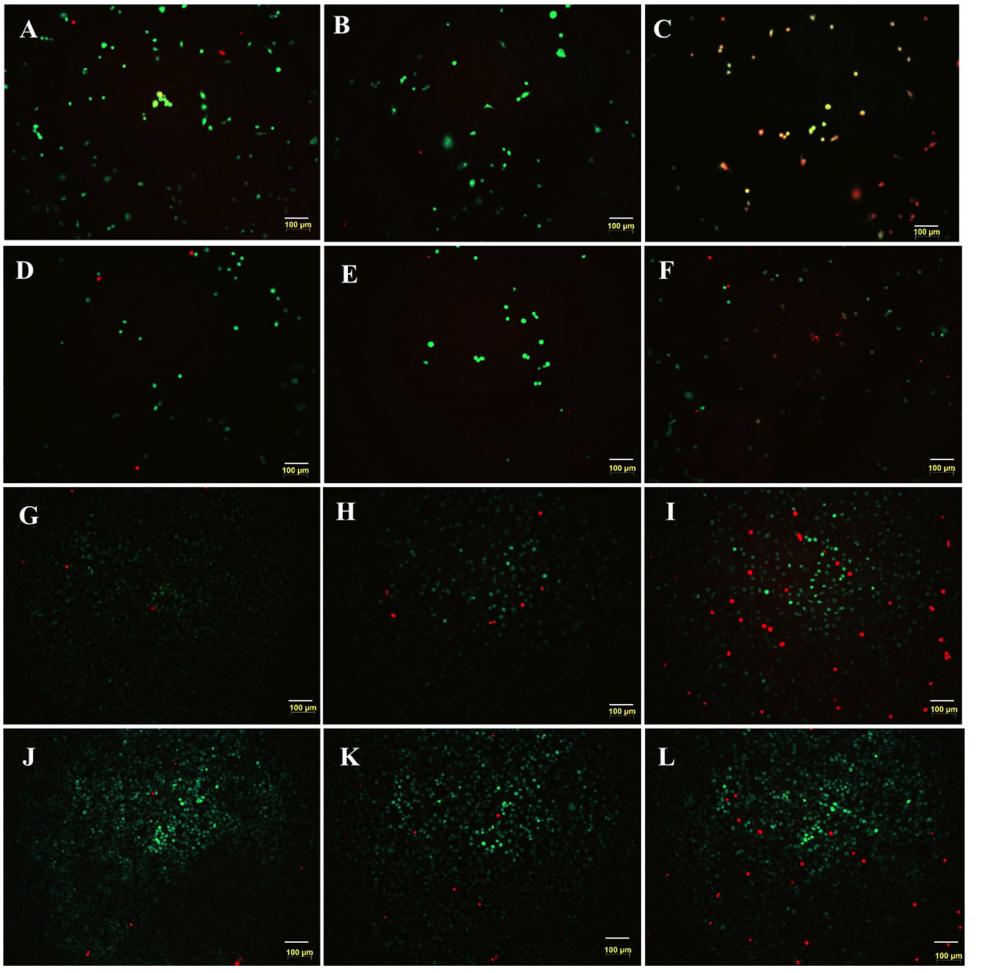

Figure 9. Fluorescent micrographs of calcein AM/ethidium bromide double-stained HepG2 (A-F) and L929 (G-L) cells treated with magnetic and nonmagnetic PLinaS-g-PEG-NPs. Control (A, G), MNPs (B, H), PLinaS-g-PEG–NPs (C, I), 5PLinaS-g-PEG–NPs (D, J), 7PLinaS-g-PEG–NPs (E, K), 10PLinaS-g-PEG–NPs (F, L). Scale bar is 100 µm.

Flow cytometer analysis

Apoptotic or necrotic cell death induced by the PLinaS-g-PEG-NPs was investigated further using flow cytometer. As can be seen in Figure 11, a typical dot plot shows three main populations; Q3 quadrant represents viable cells (Annexin V-negative/propidium iodide negative), Q4 quadrant shows early apoptotic cells (Annexin V-positive/propidium iodide negative), and Q2 quadrant represents cells in late apoptosis and necrosis phase (Annexin V-positive/propidium iodide positive).

Many studies related to the evaluation toxicity of iron oxide nanoparticles against cancer cells have already published. The studies support that the cells exposed to iron oxide particles induced apoptosis [48]. In evaluation of the flow cytometry analysis data obtained in this study, after 24-h incubation with HepG2, MNPs-encapsulated PLinaS-g-PEG-NPs groups increased apoptosis and necrosis rate depend on dose

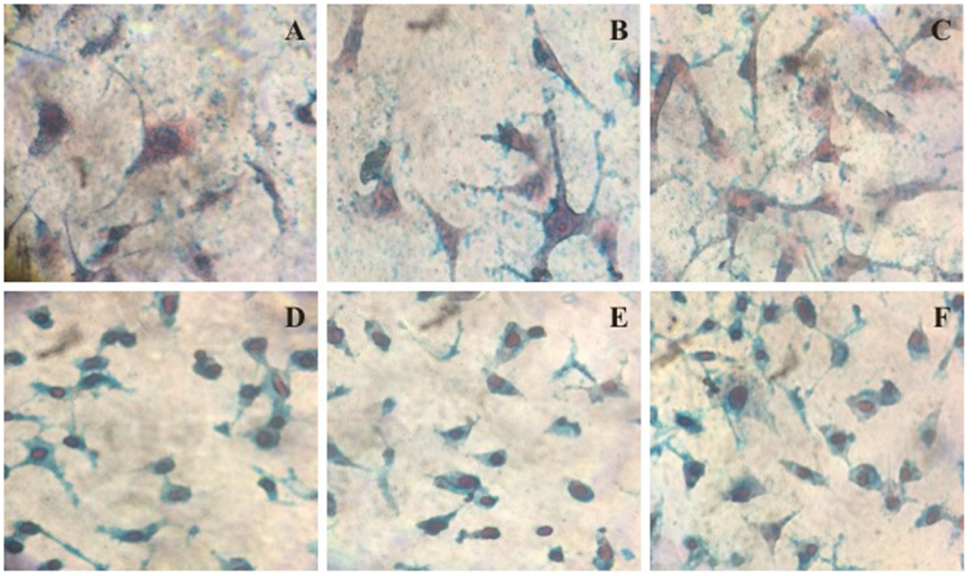

Figure 10. Prussian blue staining labelled with PLinaS-g-PEG-NPs (A, D), 7PLinaS-g-PEG-MNPs (B, E) and 10PLinaS-g-PEG-MNPs (C, F) by HepG2, and L929 cells by inverted microscope, respectively.

(Figure 11). For example, the total cell population of early apoptosis (Q3) and late apoptosis (Q2) in HepG2 cells treated with 7PLinaS-g-PEG MNPs and 10PLinaS-g-PEG MNPs were 1.8/4.7%, and 7.4/5.9%, respectively. Similarly, Huang et al. reported that malign cells (SKHep-1, HepG2, HeLa) treated with 10 nm of anionic iron oxide nanoparticles, and their findings showed that there was a strong correlation between cell death and MNPs concentration [49].

On the other hand, to further determine the cytoxicity of PLinaS-g-PEG-NPs towards healthy cell line, the same experiment was conducted on L929. The assay results showed that the percentage of necrotic cells increased depending on the concentration of encapsulated-MNPs while magnetic- or nonmagnetic PLinaS-g-PEG-NPs did not cause any apoptotic response. In the meantime, HepG2 cells exposed to PLinaS-g-PEG-NPs as compared L929 induced markedly apoptosis depend on encapsulated MNPs concentration. Annexin V-positive viable cell population is only 77% upon the treatments with 10PLinaS-g-PEG MNPs in HepG2 while the rate in L929 is 91.5%, as shown in Figure 12, indicating uptake of PLinaS-g-PEG–NPs by cancer cells was significantly higher contrary to normal mouse fibroblast cells.

Liu *et al.* designed a multifunctional composite by grafting of Fe_3O_4 nanoparticles functionalized with polyethylene imine (PEI). To evaluate *in vitro* cytotoxicity of the prepared material, L929 and HeLa cells were used, and the cell viability test results conducted using L929 showed almost a 100% viability rate [32].

Internalization studies of magnetic and nonmagnetic PLinaS-g-PEG-NPs

The internalization of NPs by HepG2, and L929 was examined in detail by confocal microscopy, and was given in Figure 13. The HepG2 cells treated with NPs

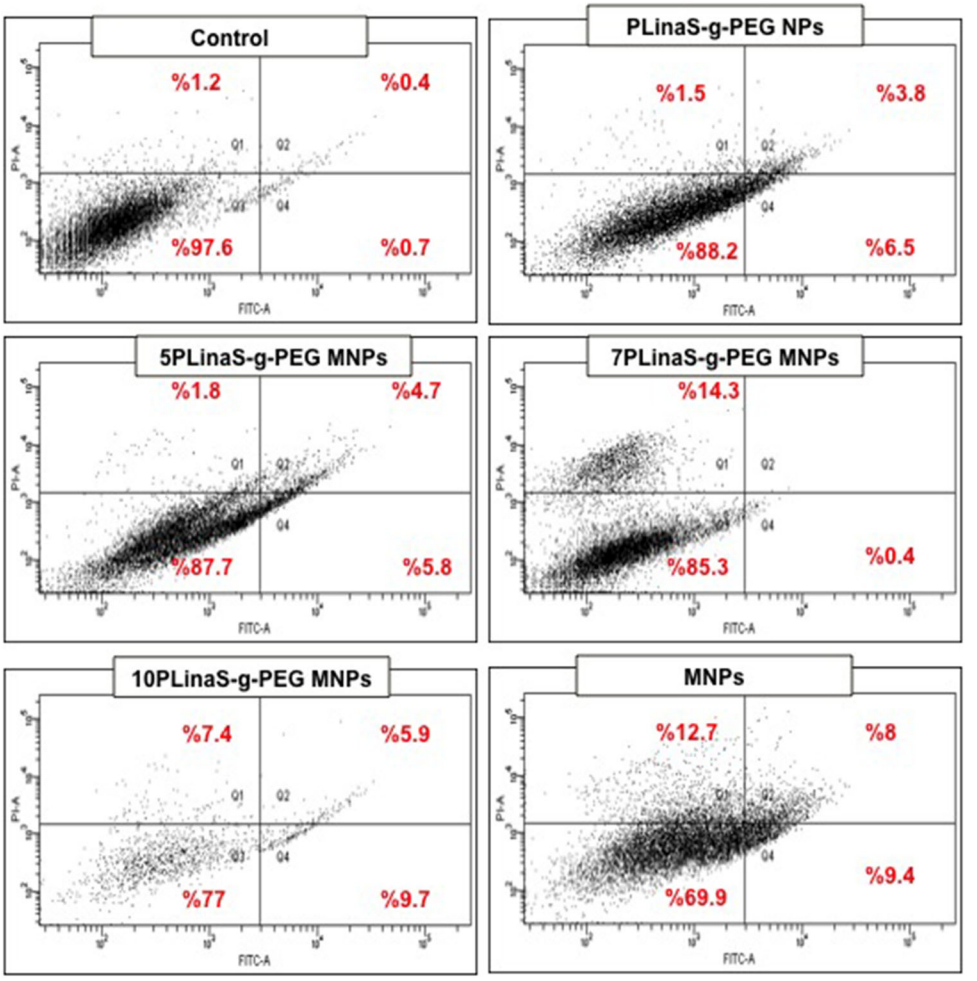

Figure 11. Measured cell mortalities data of HepG2 by flow cytometry. HepG2 cells were treated with magnetic and nonmagnetic PLinaS-g-PEG-NPs.

accumulated more intensely in the cell cytoplasm and perinuclear site. However, normal mouse fibroblast cells showed also no equal internalization, and their fluorescence signal was very low. The selective cellular uptake of NPs can be attributed to taken up of LA by hepatocytes *via* its putative plasma membrane transporter although PEGylation causes an inability in NPS-membrane interaction [50]. The results clearly showed that PLinaS-g-PEG-MNPs consisting of PEG and LA were more efficient in cancer cell targeting and internalization in HepG2 cells respect to L929.

Cholesterol analysis

Membrane cholesterol alteration in L929 and HepG2 cell lines by the synthesized PLinaS-g-PEGNPs was observed by fluorescent microscopy (Figure 14). We have also observed significant differences in the membrane cholesterol, especially in HepG2. As mentioned in earlier reports, cholesterol depletion affects the membrane structure,

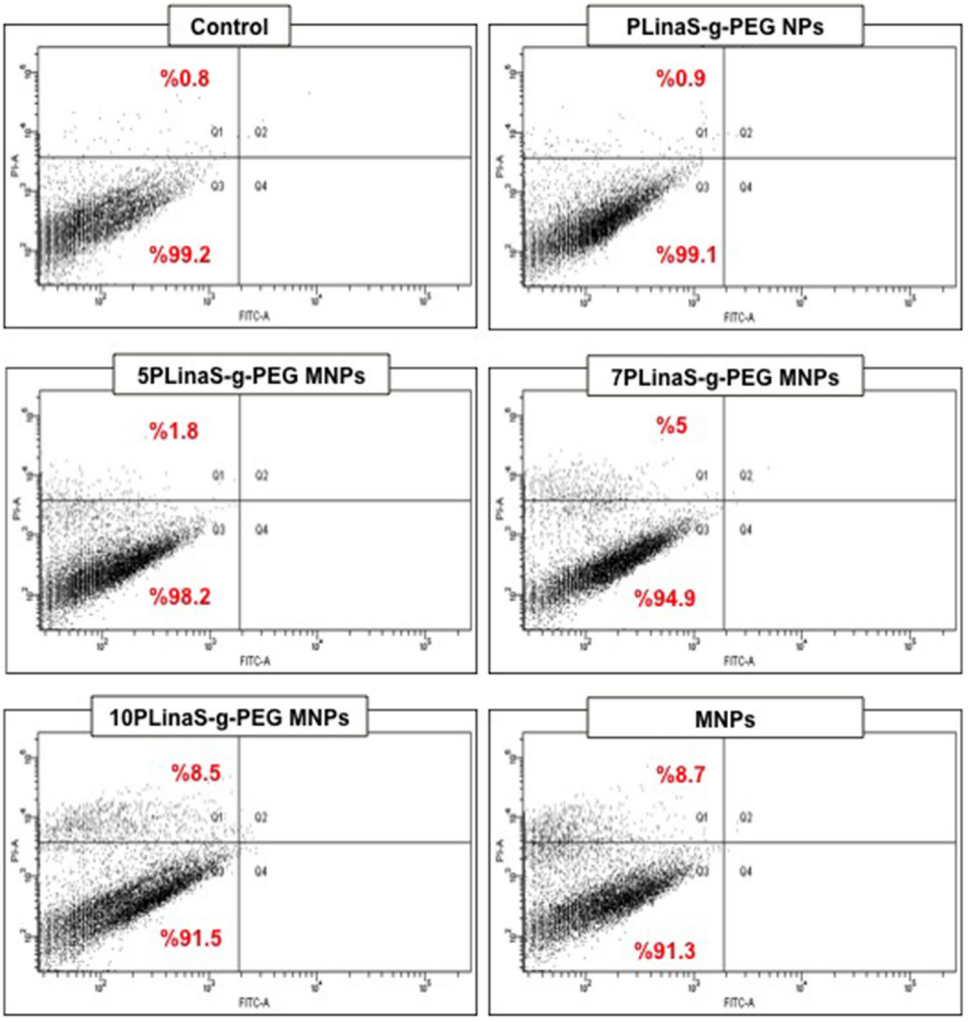

Figure 12. Measured cell mortalities data of L929 by flow cytometry. L929 cells were treated with magnetic and nonmagnetic PLinaS-g-PEG-NPs.

and so induces cell death [51]. Accordingly, we verified cholesterol depletion and consequently, cell death after treatment by various concentration of PLinaS-g-PEG MNPs while there is no significant difference in non-cancerous cell line (L929 cells) which also exposed to various concentration of PLinaS-g-PEG NPs. Lu et al. investigated the action of LA on colorectal cancer cell lines, LOVO (undifferentiated) and RKO (semi-differentiated), and the human umbilical vein endothelial cells (HUVEC) taken as normal cell control, *in vitro*. They observed that normal human umbilical vein endothelial cells (HUVEC) compared to other cell lines were less sensitive against n-6 PUFA linoleic acid (LA) (the degree of sensitivity to LA is as follows: RKO > LOVO > HUVEC) [51]. In parallel, the results obtained in this study were strongly confirmed that the linoleic acid affected the cholesterol synthesis in cancerous cells (HepG2). Earlier reports confirmed that the linoleic acid inhibited the cholesterol synthesis in HepG2 and accumulated in hepatocytes besides the plasma

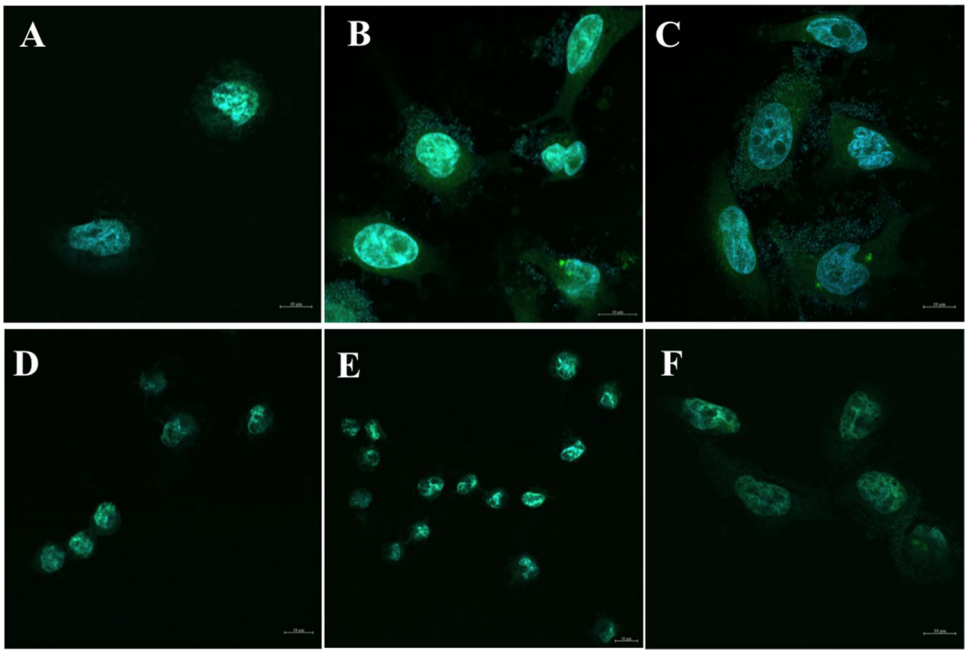

Figure 13. Internalization and uptake of PLinaS-g-PEG-NPs (A, D), 7PLinaS-g-PEG-MNPs (B, E) and 10PLinaS-g-PEG-MNPs (C, F) by HepG2, and L929 cells by confocal microscopy, respectively. Scale bar is 10 μm.

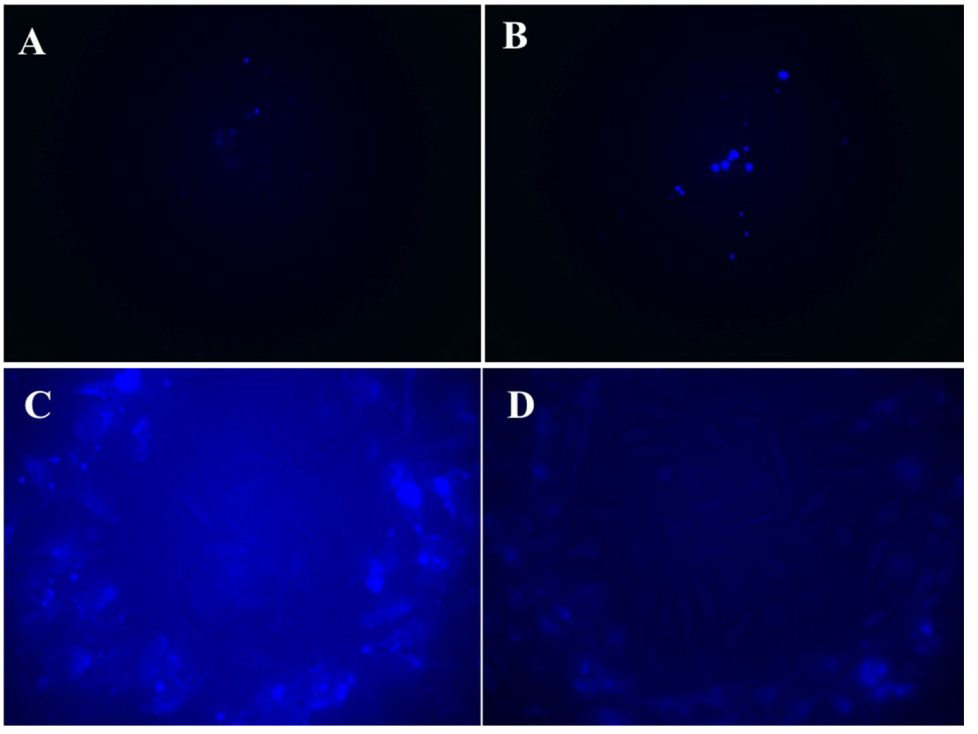

Figure 14. Accumulation of cholesterol inside HepG2 (A, B) and L929 (C, D) after treatment with 7PLinaS-g-PEG-MNPs (A, C) and 10PLinaS-g-PEG-MNPs (B, D), respectively.

cholesterol-lowering effect of linoleic acid [52,53]. Consequently, it can be concluded that linoleic acid acts as a cholesterol-depleting agent in cancer cells.

Conclusions

This study presents an extensive investigation on targeting potential of the nonmagnetic- and magnetic PLinaS-g-PEG-NPs as a function of linoleic acid and PEG- containing coatings. In summary, the synthesized PLinaS-g-PEG-MNPs were found to have spherical particle morphology with the average particle size 150–200 nm. Furthermore, HepG2 cells exposed NPs results in significant cytotoxicity with a strong apoptotic response in direct proportion to the dosage of MNPs while not in a normal mouse fibroblast cell line (L929). The cellular uptake behaviors of NPs verified that the best cellular internalization was observed in HepG2, and the tropism was facilitated by linoleic acid, and PEG-content as well as confirmed by Prussian blue staining images. Furthermore, the excellent targeting feature without need for a specific targeting ligand molecule may provide excellent sensitivity for imaging as a potential MRI contrast agent, and have promise for safe usage in anticancer therapy without killing normal mouse fibroblast cells, and should be investigated further the biocompatibility onto normal human cell lines.

Acknowledgments

The authors would like to thank Emine Ulku Sarıtas, Ergin Atalar, and Mustafa Can Delikanlı for providing comments in MRI analysis.

Disclosure statement

The authors declared no potential conflicts of interest.

Funding

This work was financially supported by Aksaray University (project no. 2017-046).

References

[1] Asham EH, Kaseb A, Ghobrial RM. Management of hepatocellular carcinoma. Surg Clin North Am. 2013;93(6):1423–1450.
[2] Allemann P, Demartines N, Bouzourene H, et al. Long-term outcome after liver resection for hepatocellular carcinoma larger than 10 cm. World J Surg. 2013; 37(2):452–458.
[3] Mohamed NK, Hamad MA, Hafez MZ, et al. Nanomedicine in management of hepatocellular carcinoma: challenges and opportunities. Int J Cancer. 2017;140(7):1475–1484.
[4] Zhang X, Ng HL, Lu A, et al. Drug delivery system targeting advanced hepatocellular carcinoma: current and future. Nanomedicine. 2016;12(4):853–869.
[5] Gupta AK, Gupta M. Synthesis and surface engineering of iron oxide nanoparticles for biomedical applications. Biomaterials. 2005;26(18):3995–4021.
[6] Jordan A, Wust P, Scholz R, et al. Scientific and clinical applications of magnetic carriers. edited by U. Hafeli, W. Shutt, J. Teller, and M. Zborowski. Plenum, New York, 1997.

[7] Clift MJ, Rothen-Rutishauser B, Brown DM, et al. The impact of different nanoparticle surface chemistry and size on uptake and toxicity in a murine macrophage cell line. Toxicol Appl Pharmacol. 2008;232(3):418–427.
[8] Sun C, Lee JSH, Zhang MQ. Magnetic nanoparticles in MR imaging and drug delivery. Adv Drug Deliv Rev. 2008;60(11):1252–1265.
[9] Chouly C, Pouliquen D, Lucet I, et al. Development of superparamagnetic nanoparticles for MRI: effect of particle size, charge and surface nature on biodistribution. J Microencapsul. 1996;13(3):245–255.
[10] Moghimi SM, Hunter AC, Murray JC. Long-circulating and target- specific nanoparticles: theory to practice. Pharmacol Rev. 2001;53(2):283–318.
[11] Lee JH, Huh YM, Jun YW, et al. Artificially engineered magnetic nanoparticles for ultra-sensitive molecular imaging. Nat Med. 2007;13(1):95–99.
[12] Bonnemain B. Superparamagnetic agents in magnetic resonance imaging: physicochemical characteristics and clinical applications. A review. J Drug Target. 1998;6(3): 167–174.
[13] Goya GF, Grazú V, Ibarra MR. Magnetic nanoparticles for cancer therapy. CNANO. 2008;4(1):1–16.
[14] Ma HL, Qi XR, Maitani Y, et al. Preparation and characterization of superparamagnetic iron oxide nanoparticles stabilized by alginate. Int J Pharm. 2007;333(1-2):177–186.
[15] Müller K, Skepper JN, Posfai M, et al. Effect of ultrasmall superparamagnetic iron oxide nanoparticles (Ferumoxtran-10) on human monocyte-macrophages in vitro. Biomaterials. 2007;28(9):1629–1642.
[16] Sun C, Sze R, Zhang M. Folic acid-PEG conjugated superparamagnetic nanoparticles for targeted cellular uptake and detection by MRI. J Biomed Mater Res A. 2006;78(3): 550–557.
[17] Lutz JF, Stiller S, Hoth A, et al. One-pot synthesis of pegylated ultrasmall iron-oxide nanoparticles and their in vivo evaluation as magnetic resonance imaging contrast agents. Biomacromolecules. 2006;7(11):3132–−3138.
[18] Lopez-Cruz A, Barrera C, Calero-Ddelc VL, et al. Water dispersible iron oxide nanoparticles coated with covalently linked chitosan. J Mater Chem. 2009;19(37):6870–6876.
[19] Mao S, Neu M, Germershaus O, et al. Influence of polyethylene glycol chain length on the physicochemical and biological properties of poly(ethylene imine)-graft-poly(ethylene glycol) block copolymer/SiRNA polyplexes. Bioconjug Chem. 2006;17(5):1209–1218.
[20] Maeda H. Tumor-selective delivery of macromolecular drugs via the EPR effect: background and future prospects. Bioconjug Chem. 2010;21(5):797–802.
[21] Khandhar AP, Keselman P, Kemp SJ, et al. Evaluation of PEG-coated iron oxide nanoparticles as blood pool tracers for preclinical magnetic particle imaging. Nanoscale. 2017;9(3):1299–1306.
[22] Giudetti AM, Beynen AC, Lemmens AG, et al. Hepatic lipid and carbohydrate metabolism in rats fed a commercial mixture of conjugated linoleic acids (Clarinol G-80). Eur J Nutr. 2005;44(1):33–39.
[23] Ferramosca A, Savy V, Conte L, et al. Conjugated linoleic acid and hepatic lipogenesis in mouse: role of the mitochondrial citrate carrier. J Lipid Res. 2006;47(9):1994–2003.
[24] Yotsumoto H, Hara E, Naka S, et al. 10*trans*, 12*cis*-Linoleic acid reduces apolipoprotein B secretion in HepG2 cells. Food Res Int. 1998;31(5):403–409.
[25] Pandey NR, Renwick J, Misquith A, et al. Linoleic acid-enriched phospholipids act through peroxisome proliferator-activated receptors alpha to stimulate hepatic apolipoprotein A-I secretion. Biochemistry. 2008;47(6):1579–1587.
[26] Ince O, Akyol E, Sulu E, et al. Synthesis and characterization of novel rod-coil (tadpole) poly(linoleic acid) based graft copolymers. J Polym Res. 2016;23(1):5.
[27] Karahaliloğlu Z, Yalçın E, Demirbilek M, et al. Magnetic silk fibroin e-gel scaffolds for bone tissue engineering applications. J Bioactive Comp Polym. 2017;32(6):596–614.

[28] Varshosaz J, Sadeghi-Aliabadi H, Ghasemi S, et al. Use of magnetic folate-dextran-retinoic acid micelles for dual targeting of doxorubicin in breast cancer. Biomed Res Int. 2013;2013: 680712
[29] Souza TGF, Ciminelli VST, Mohallem N. A comparison of TEM ad DLS methods to characterize size distribution of ceramic nanoparticles. J Phys Conf Ser. 2016; 733: 012039.
[30] Nafee N, Schneider M, Schaefer UF, et al. Relevance of the colloidal stability of chitosan/PLGA nanoparticles on their cytotoxicity profile. Int J Pharm. 2009;381(2):130–139.
[31] Yue Z-G, Wei W, Lv P-P, et al. Surface charge affects cellular uptake and intracellular trafficking of chitosan-based nanoparticles. Biomacromolecules. 2011;12(7):2440–2446.
[32] Liu X, Kaminski MD, Guan Y, et al. Preparation and characterization of hydrophobic superparamagnetic magnetite gel. J Magn Magn Mater. 2006;306(2):248–253.
[33] Wei S, Zhu Y, Zhang Y, et al. Preparation and characterization of hyperbranched aromatic polyamides/Fe_3O_4 magnetic nanocomposite. React Funct Polym . 2006;66(11): 1272–1277.
[34] Fukuchi T. Dr. Sebastiano D'Amico (Ed.) In-Tech Publication. 2012. ISBN: 978-953-307-991-2.
[35] Koseoglu Y, Aktas B. Surface effects on magnetic properties of superparamagnetic magnetite nanoparticles. Phys Stat Sol (c). 2006;1:3516–3520.
[36] Mu X, Yan C, Tian Q, et al. BSA-assisted synthesis of ultrasmall gallic acid-Fe(III) coordination polymer nanoparticles for cancer theranostics. Int J Nanomedicine. 2017; 12:7207–7223.
[37] Berridge MV, Tan AS. Characterization of the cellular reduction of 3-(4,5-dimethylthiazol-2-yl)-2,5-diphenyltetrazolium bromide (MTT): subcellular localization, substrate dependence, and involvement of mitochondrial electron transport in MTT reduction. Arch Biochem Biophys. 1993;303(2):474–482.
[38] Pisanic TR, Jin S, Shubayev VI. Iron Oxide Magnetic Nanoparticle Nanotoxicity. In: Sahu SC, Asciano DA, editors. Incidence and mechanisms, in nanotoxicity. Chichester: John Wiley & Sons, Ltd, 2009. pp. 298–425.
[39] Bae S, Lee S, Hirukawa A, et al. AC magnetic-field-induced heating and physical properties of ferrite nanoparticles for a hyperthermia agent in medicine. IEEE Trans. Nanotechnol. 2009;8:86–94.
[40] Giri J, Pradhan P, Sriharsha T, et al. Preparation and investigation of potentiality of different soft ferrites for hyperthermia applications. J Appl Phys . 2005;97(10): 10Q916–10Q913.
[41] Tomitaka A, Hirukawa A, Yamada T, et al. Biocompatibility of various ferrite nanoparticles evaluated by *in vitro* cytotoxicity assays using HeLa cells. J Magn Magn Mater . 2009;321(10):1482–1484.
[42] Jeng HA, Swanson J. Toxicity of metal oxide nanoparticles in mammalian cells. J Environ Sci Health A Tox Hazard Subst Environ Eng. 2006;41(12):2699–2711.
[43] Au C, Mutkus L, Dobson A, et al. Effects of nanoparticles on the adhesion and cell viability on astrocytes. Biol Trace Elem Res. 2007;120(1-3):248–225.
[44] Igarashi M, Miyazawa T. The growth inhibitory effect of conjugated linoleic acid on a human hepatoma cell line, HepG2, is induced by a change in fatty acid metabolism, but not the facilitation of lipid peroxidation in the cells. Biochim Biophys Acta. 2001; 1530(2-3):162–171.
[45] Mishra P, Nayak B, Dey RK. PEGylation in anti-cancer therapy: an overview. Asian J Pharm Res. 2016;11(3):337–348.
[46] Begin ME, Ells G, Das UN, et al. Differential killing of human carcinoma cells supplemented with n-3 and n-6 polyunsaturated fatty acids. J Natl Cancer Inst. 1986;77(5): 1053–1062.
[47] Yang L, Mao H, Cao Z, et al. Molecular imaging of pancreatic cancer in an animal model using targeted multifunctional nanoparticles. Gastroenterology. 2009;136(5): 1514–1525.

[48] Orrenius S, Nicotera P, Zhivotovsky B. Cell Death Mechanisms and Their Implications in Toxicology. Toxicol Sci. 2011;119(1):3–19.
[49] Huang C-Y, Ger T-R, Wei Z-H, et al. Compare analysis for the nanotoxicity effects of different amounts of endocytic iron oxide nanoparticles at single cell level. PLoS ONE. 2014;9(5):e96550
[50] Schürer NY, Stremmel W, Grundmann JU, et al. Evidence for a novel keratinocyte fatty acid uptake mechanism with preference for linoleic acid: comparison of oleic and linoleic acid uptake by cultured human keratinocytes, fibroblasts and a human hepatoma cell line. Biochim Biophys Acta . 1994;1211(1):51–60.
[51] Lu X, Yu H, Ma Q, et al. Linoleic acid suppresses colorectal cancer cell growth by inducing oxidant stress and mitochondrial dysfunction. Lipids Health Dis. 2010;9:106
[52] Rassias G, Kestin M, Nestel PJ. Linoleic acid lowers LDL cholesterol without a proportionate displacement of saturated fatty acid. Eur J Clin Nutr. 1991;45(6):315–320.
[53] Fukumitsu S, Villareal MO, Onaga S, et al. α-Linolenic acid suppresses cholesterol and triacylglycerol biosynthesis pathway by suppressing SREBP-2, SREBP-1a and -1c expression. Cytotechnology. 2013;65(6):899–907.